

Low-energy ($e,2e$) spectroscopy from the W(001) surface: Experiment and theory

R. Feder, H. Gollisch, D. Meinert, and T. Scheunemann

Theoretische Festkörperphysik, Universität Duisburg, D-47048 Duisburg, Germany

O. M. Artamonov, S. N. Samarin, and J. Kirschner

Max-Planck-Institut für Mikrostrukturphysik, 06120 Halle, Weinberg 2, Germany

(Received 2 June 1998)

The simultaneous ejection of two electrons from the (001) surface of W due to the collision of incident low-energy electrons with valence electrons has been studied experimentally and theoretically. Energy and momenta of the ejected electrons were measured simultaneously by a combination of coincidence and time-of-flight techniques. Calculations were performed in a relativistic distorted-wave Born approximation including exchange, in which the primary electron and the two emitted electrons are described by quasiparticle multiple scattering states. The valence electron is represented by linear combinations of Bloch waves matched at the surface. Screened Coulomb interaction matrix elements between these four states are evaluated. Experimental and calculated energy distributions from W(001) for very-low-energy primary electrons at normal and grazing incidence are in fairly good overall agreement. Although some features of one-dimensional bulk densities of states are roughly reflected, Coulomb matrix elements with low-energy-electron-diffraction-type states play a vital role. Further analysis reveals in detail the importance of elastic scattering of the primary electron and of the two ejected electrons. Some observed features can be attributed to occupied surface states.

[S0163-1829(98)05848-2]

I. INTRODUCTION

Among the various possible reaction channels of an electron with a solid target, a particularly important one involves a single collision event with a valence electron resulting in two electrons leaving the solid. Energy- and momentum-resolved observation of these two electrons, so-called ($e,2e$) spectroscopy, is well established in the transmission mode using high-energy primary electrons (cf., e.g., Refs. 1 and 2 and references therein). Since at high energies the primary electron and the two final-state electrons are to a good approximation represented by plane waves, the Coulomb scattering cross section is simple to evaluate and reveals the momentum density of the valence electrons.

At low primary energies (less than a few 100 eV), however, the primary and the two outgoing electron states involve, as is well known from low-energy electron diffraction (LEED), strong elastic multiple scattering by the ion cores. For the ($e,2e$) scattering cross section, this implies that its theoretical treatment is more complicated³⁻⁵ and its physical interpretation far less straightforward. Experimentally, low-energy reflection mode ($e,2e$) spectroscopy made substantial progress fairly recently (cf. Refs. 6-9 and references therein). In particular, a time-of-flight technique made it possible to measure simultaneously energies and momenta of two electrons emerging in coincidence.⁷

In view of gaining more insight into the very-low-energy ($e,2e$) process itself and of exploring its information potential on surface systems, we carried out an extensive joint experimental and theoretical study of the ($e,2e$) cross section for electrons with energies below 25 eV incident on a clean W(001) surface. Our first aim has been to establish the level of agreement between experimental data and their calculated counterparts. Since our theory involves only a single

collision event between the primary electron and a valence electron, this agreement should reveal to what extent the present experimental setup actually detects such single collisions relative to accidental coincidences. Since our formalism accounts for all elastic scattering events of the primary and of the two outgoing electrons with the ion cores, the importance of specific elastic events (e.g., specular or non-specular reflection of the primary electron, specular or non-specular reflection of one or of both outgoing electrons) can be determined by additional calculations ("computer experiments"), in which elastic scattering amplitudes are selectively switched off.

The paper is organized as follows. The experimental and theoretical methods are described in Secs. II and III, respectively. Section IV addresses, with the aid of various model calculations, the interpretation of ($e,2e$) cross sections and the physical information obtainable from them. In Sec. V, we present and discuss experimental and theoretical results for normal and for grazing incidence on W(001).

II. EXPERIMENTAL DETAILS

Our low-energy electron coincidence experiments were carried out in a μ -metal vacuum chamber with a vacuum in the range of 10^{-11} Torr. The experimental setup is shown in Fig. 1. A single crystal of tungsten (001) was mounted on a rotatable holder. The sample cleaning procedure included the oxidation of the sample followed by high-temperature flashes to remove carbon from the sample surface. The cleanliness of the surface was monitored by Auger spectroscopy. We used two multichannel plates (MCP) 75 mm in diameter with resistive anodes as position sensitive electron detectors. The detectors and the electron gun were coplanar with the surface normal and the [100] direction along the surface. The direc-

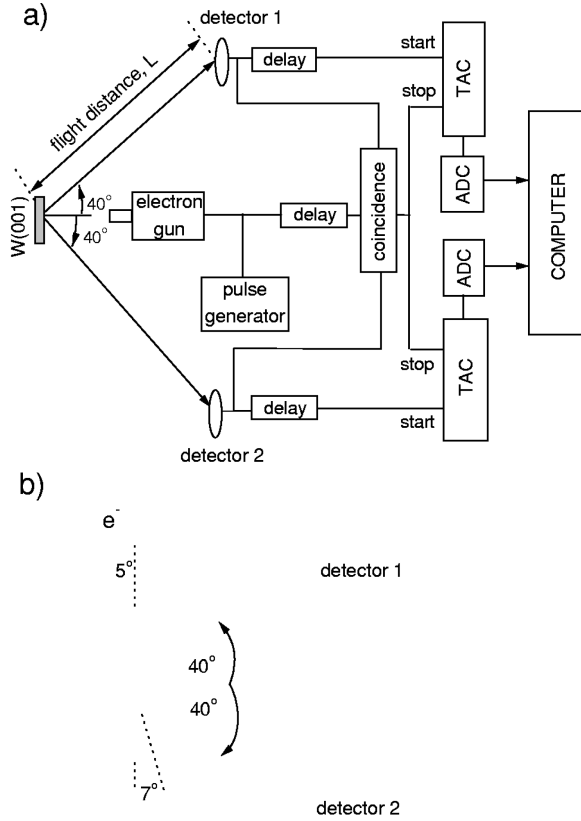


FIG. 1. Experimental setup of the ($e,2e$) time-of-flight spectrometer. ADC is analog-to-digital converter, TAC is the time-to-amplitude converter. (a) Normal incidence; (b) grazing incidence. The flight times of the two electrons are determined by two time-to-amplitude converters (TAC) and fed into the computer via two analog-to-digital converters (ADC). A fast “coincidence” circuitry accepts two-electron events only if they fall within a 200 ns time window.

tion of the primary beam was chosen first normal to the surface and second at a polar angle of 88° with respect to the surface normal (i.e., grazing incidence with a glancing angle of 2°). In the case of normal incidence, the electron gun axis was aligned along the bisector of the 80° angle between the detectors [Fig. 1(a)]. For the grazing incidence geometry, the electron gun axis was rotated in the plane of detectors away from the previous direction by 95° [Fig. 1(b)]. The distance L between the sample and the detectors could be varied from 130 mm to 260 mm. The position-sensitive detectors allowed us to control the electron beam position on the sample observing the specular beam as well as diffracted beams. The electron beam diameter on the sample was less than 1 mm. Though the position-sensitive detection in principle provides angular resolution, at the present stage of experiments this feature was not used explicitly because of the concomitant loss of counting statistics.

In order to measure the energies of both correlated electrons generated by one incident electron, we combined the coincidence technique with a time-of-flight electron energy measurement. The incident electron current was of the order of 10^{-14} A on average. It was pulsed with a width of about 1 ns and a repetition rate of 2.5×10^6 Hz using a pulse generator. The trigger pulse from the generator was used as a reference point on the time-of-flight scale. If one of the channel

plates is hit by an electron, a fast pulse starts one of the time-to-amplitude converters (TAC). If subsequently the other channel plate is hit by another electron, it starts the other TAC. If two delayed shaped pulses from the detectors and the delayed trigger pulse from the generator coincide within a time window of 200 ns, a logic unit delivers a stop pulse to each TAC. The times of flight of the two electrons are then recorded as a point in a two-dimensional time-of-flight coordinate system. This point represents a valid ($e,2e$) event. If an electron (with rest mass m) takes the time T to pass the distance L between the sample and one of the detectors, its kinetic energy in the presently relevant nonrelativistic limit is

$$E = \frac{m \left(\frac{L}{T} \right)^2}{2}. \quad (1)$$

The energy resolution δE of the time-of-flight energy measurement is obtained from Eq. (1) as

$$\delta E = \frac{2}{L} \sqrt{\frac{2}{m}} E^{3/2} \delta T. \quad (2)$$

In our setup, the time resolution δT in Eq. (1) is essentially determined by the primary electron pulse width, i.e., $\delta T = 1$ ns. With $L = 260$ mm, we obtain $\delta E = 0.05$ eV for the typical energy $E = 5$ eV. An independent experimental check of the energy resolution δE in the energy range 4–5 eV yields, however, $\delta E = 0.4$ eV, which is approximately equal to the half-width of the electron energy distribution in the incident electron beam. This means that at low energies the energy resolution is not limited by the time resolution but by the energy spread of the incident electron beam.

In the present experiment we measured the relative time of flight T of electrons with respect to the arrival time of elastically reflected primary electrons. For calibration we determined the kinetic energy $E_p = E_1$ of the primary electrons on the base of Eq. (1) by measuring the relative time of flight of elastically scattered electrons ΔT for different distances of flight $\Delta L = L_1 - L_2$. This value of E_p was then used as a reference to calibrate the energy scale of the time-of-flight analyzers. The zero point on the time-of-flight scale thus corresponds to the arrival time of elastically reflected primary electrons. Any other point represents the relative flight time T of a slower electron generated by an incident electron. By virtue of Eq. (1) one easily obtains

$$T = L \left(\sqrt{\frac{m}{2E}} - \sqrt{\frac{m}{2E_p}} \right), \quad (3)$$

from which

$$E = \frac{m \left(\frac{T}{L} + \sqrt{\frac{m}{2E_p}} \right)^{-2}}{2}. \quad (4)$$

This equation is used to convert the time-of-flight scale T to the energy scale E .

In Fig. 2(a) we show, as an example, the two-dimensional time-of-flight distribution of correlated electron pairs obtained from W(001) in our normal-incidence geometry for primary electron energy $E_p = 20$ eV. The distance L between sample and detectors was 140 mm. We integrated over the

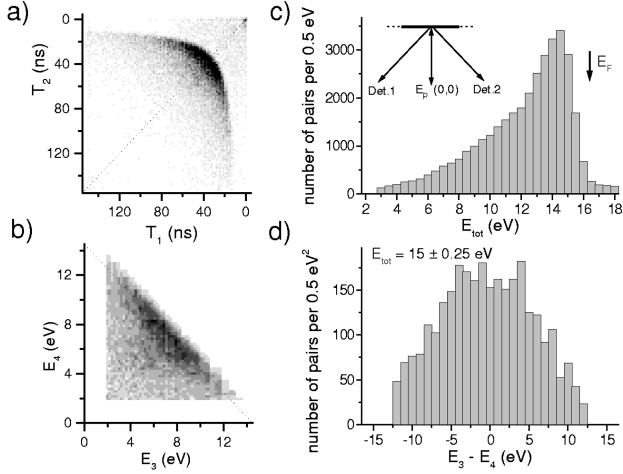


FIG. 2. Time-of-flight and energy distributions of correlated electron pairs for normal incidence of electrons with energy $E_p = 20$ eV. (a) Two-dimensional time-of-flight distribution of correlated electrons. The black point in the upper right corner corresponds to the accidental coincidence of two elastically reflected electrons and serves as a calibration point. (b) Two-dimensional energy distribution of correlated electrons. (c) Histogram of the correlated pairs distribution as a function of the total energy E_{tot} of a pair. The height of a column represents the number of events within the total energy band $E_{\text{tot}} \pm 0.25$ eV. (d) Energy sharing distribution of correlated pairs with a given total energy. The height of a column represents the number of pairs with the energy difference $E_1 - E_2$ within the total energy band $E_{\text{tot}} = 15 \pm 0.25$ eV.

acceptance cones of the detectors ($\Omega = 0.21$ sr) without making corrections for the slightly different flight paths for the different angles. The coincidence events are displayed by a two-dimensional gray-scale plot, in which black corresponds to the highest number of events. A ridgelike maximum in this plot represents the most probable combinations of electron energies within time-correlated electron pairs. The distribution looks quite symmetric with respect to the diagonal (dashed line) of the frame. Points on this line represent correlated pairs with equal times of flight of both electrons, i.e., with equal energies.

The energy distribution of electron pairs, which is obtained from the time-of-flight distribution in Fig. 2(a) by means of Eq. (4), is shown in Fig. 2(b). The ridgelike maximum of the time-of-flight distribution is seen to be transformed into a diagonal band along the line $E_3 + E_4 = 14.5$ eV in the energy distribution. If we take the width of this band equal to 0.5 eV, then within this band the sum of the energies of two correlated electrons (we call it “total energy” of a pair) is equal to $E_{\text{tot}} = 14 \pm 0.25$ eV. Let us now focus on true ($e, 2e$) events, in which the detected electrons are produced in single collision between the incident electron and a target electron. From the total energy E_{tot} of a pair and the incident electron energy $E_p = E_1 = 20$ eV, energy conservation then yields the binding energy $E_b = E_2$ of the target electron as $E_b = E_2 = E_1 - E_3 - E_4 = E_p - E_{\text{tot}} = 20 - 14.5 = 5.5$ eV. Since the work function of W(001) is 4.6 eV, this implies that the creation of correlated pairs is most likely for target electrons with energies just below the Fermi level.

From the above energy distribution we calculated the number of events in a total energy band $E_{\text{tot}} = (E_3 + E_4)$

± 0.25 eV as a function of E_{tot} . This “total energy distribution” is shown in Fig. 2(c). Its maximum corresponds to target electron excitation from energy levels just below the Fermi level. These electron pairs must have been created in a single-step process, because any additional inelastic scattering would have decreased the total energy of the pairs. Correlated electron pairs with lower total energies may originate either from the excitation of bound electrons in deeper energy levels or from a multistep electron-electron scattering process.

For quantitative analysis and comparison with theoretical results it is particularly useful to plot, for a sequence of fixed values of $E_{\text{tot}} = E_3 + E_4$, the number of pairs with energy difference $\Delta = E_3 - E_4$ within an energy band centered at E_{tot} . As an example for such energy sharing distributions, we show in Fig. 2(d) the one obtained from the data of Fig. 2(b) for the total energy band $E_3 + E_4 = 15 \pm 0.25$ eV. It is seen to be symmetric with respect to the energy difference $E_3 - E_4 = 0$. This symmetry corresponds to the symmetry of the energy distribution in Fig. 2(b) with respect to the $E_3 = E_4$ line, which is dictated by the geometrical symmetry of our normal-incidence setup.

III. THEORY

Our numerical calculations of ($e, 2e$) from W(001) are based on a theoretical approach, which has been outlined in Ref. 3. In the following, we present more details and specify particular model assumptions for the subsequent computations.

For a primary electron, which at the source has kinetic energy E_1 and momentum \mathbf{k}_1 , colliding with a valence electron (with $E_2 < E_F$, where E_F is the Fermi energy), we are interested in the probability that one electron arrives at the first detector with kinetic energy E_3 and momentum \mathbf{k}_3 , and a second one at the second detector with E_4 and \mathbf{k}_4 . Disregarding reaction channels, in which any of these electrons loses energy to the “rest of the world,” we have energy conservation $E_1 + E_2 = E_3 + E_4$.

Denoting the time-independent initial two-electron state by $|12\rangle$, the final state by $|34\rangle$, and the electron-electron interaction Hamiltonian by H_{ee} , the transition probability to first order in H_{ee} is determined by

$$W_{34,12} = |\langle 34 | H_{ee} | 12 \rangle|^2 \delta(E_1 + E_2 - E_3 - E_4). \quad (5)$$

In each of the two-electron states, we neglect—on the grounds of screening inside the metal—interaction between the two electrons except for exchange. Consequently, we express them as antisymmetrized products of one-electron states $\psi_i(\mathbf{x})$ with $i = 1, 2, 3, 4$:

$$|ij\rangle = [\psi_i(\mathbf{x})\psi_j(\mathbf{x}') - \psi_j(\mathbf{x})\psi_i(\mathbf{x}')]/\sqrt{2} \quad (6)$$

with $(i, j) = (1, 2)$ or $(3, 4)$.

The one-electron states are obtained as follows. The interaction of each of the four electrons with the nuclei and the ground-state electrons of the target is described by an optical potential, which has lattice periodicity in the half-space occupied by the target crystal. Because of the very low electron energies in the present study, one might think of using the

Schrödinger equation. However, spin-orbit coupling and further relativistic effects are known to be important at these energies in low-energy electron diffraction (LEED), in the valence electronic structure and consequently, e.g., in photoemission (see, e.g., Refs. 10 and 11). We therefore employ a one-electron Dirac equation with the above optical potential. Consequently, the $\psi_i(\mathbf{x})$ are four-spinors, i.e., implicitly contain the electron spin. Although in the present experiment the primary electrons are unpolarized and the spin of the outgoing ones is not analyzed, it is therefore necessary to first calculate the cross sections for all the possible polarization combinations and subsequently to sum over them. For each electron, we thus have to consider two four-spinor solutions $\psi_i^{\sigma_i}(\mathbf{x})$ characterized by the label $\sigma_i = \pm$. The primary electron states $\psi_1^{\sigma_1}(\mathbf{x})$ with $\sigma_1 = \pm$ have the boundary condition that the spin at the source is up/down (relative to a chosen quantization axis). Likewise, the outgoing electrons have spin orientations $\sigma_3 = \pm$ and $\sigma_4 = \pm$ at the detectors.

Lattice periodicity parallel to the surface implies that the surface-parallel momenta \mathbf{k}_i^{\parallel} with $i = 1, 2, 3, 4$ are good quantum numbers characterizing the one-electron states. \mathbf{k}_1^{\parallel} and $\mathbf{k}_{3,4}^{\parallel}$ are given as the projections of the primary and the detected electron momenta, respectively, onto the surface. The matrix elements [Eq. (5)] are nonzero only if

$$\mathbf{k}_1^{\parallel} + \mathbf{k}_2^{\parallel} = \mathbf{k}_3^{\parallel} + \mathbf{k}_4^{\parallel}, \quad (7)$$

i.e., there is conservation of the surface-parallel momentum. Since bound states with k_2^{\parallel} (e.g., in the first Brillouin zone) and those with $k_2^{\parallel} + \mathbf{g}$, where \mathbf{g} is a surface reciprocal-lattice vector, are identical, the above conservation is actually modulo \mathbf{g} . Since there is no lattice periodicity perpendicular to the surface, the normal momentum components k_i^z are not good quantum numbers.

For the actual calculation of the $\psi_i^{\sigma_i}(\mathbf{x})$ we use a relativistic layer-KKR-method (cf. Ref. 10) with the appropriate boundary conditions. The primary electron state $\psi_1^{\sigma_1}(\mathbf{x})$ is the usual relativistic LEED state. The two outgoing electrons are described by time-reversed LEED states $\psi_i^{\sigma_i}(\mathbf{x})$ with $i = 3, 4$. To obtain the valence electron states $\psi_2^{\sigma_2}(\mathbf{x})$, we first calculate the bulk Bloch waves (by diagonalizing the layer transfer matrix). Each Bloch wave with energy E_2 , crystal momentum (k_2^{\parallel}, k_2^z), and spin label σ_2 , which propagates from the interior outward towards the surface, is then

matched at the surface with linear combinations of inward-propagating and decaying Bloch waves and with linear combinations of decaying plane waves on the vacuum side. This leads to $2n$ independent half-space solutions $\psi_2^{n\sigma_2}(\mathbf{x})$, where the index n corresponds to the outward-propagating bulk Bloch waves pairs.

While the LEED state and the time-reversed ones can be calculated for a potential containing an imaginary part (to account for finite electron lifetime), normalizable bound states $\psi_2^{n\sigma_2}(\mathbf{x})$ exist only for real potentials. Hole lifetime effects can therefore not be included *a priori*. Instead, we take them into account *ex post* by a Lorentzian convolution of the transition probability. The adequacy of this approach is suggested by photoemission results: intensities and spin polarizations from calculations using the above Bloch wave matching initial state and subsequent convolution (cf. Refs. 12–14) are practically identical with those obtained by calculations¹⁵ employing a Green-function treatment of the valence electrons (cf. Ref. 16 and references therein), which includes hole lifetime from the start. It should be noted, however, that the Bloch wave matching treatment of the valence electrons becomes impracticable for surface states. Since for real potential these are very sharp in energy, an extremely fine energy mesh is required to find them.

In the interaction Hamiltonian H_{ee} of the incident electron with a particular valence electron, we discard magnetic and retardation effects (as are, e.g., approximated by the Breit Hamiltonian), since they should be small in collisions at the present low energies. An order of magnitude estimate has, in the context of relativistic electron-atom scattering, been made in Ref. 17. We are thus left with a Coulomb interaction, which is screened by the ground-state electrons of the metal. Assuming this screening as static, we have

$$H_{ee} = V(\mathbf{x}, \mathbf{x}') = \frac{e^{-|\mathbf{x}-\mathbf{x}'|/\lambda}}{|\mathbf{x}-\mathbf{x}'|}. \quad (8)$$

We now substitute H_{ee} and the antisymmetrized four-spinor products into Eq. (5) and sum over the valence states. Since in the present experiment the primary electron beam is unpolarized and the outgoing electrons are not spin-analyzed, we furthermore sum over the spin labels σ_1, σ_3 , and σ_4 . For given primary electron energy and momentum, we thus obtain the following expression for the ($e, 2e$) transition probability:

$$W(3,4) = \sum_{\sigma_1, \sigma_3, \sigma_4} \sum_{E_2, \mathbf{k}_2^{\parallel}, n\sigma_2} |f_{\sigma_1, n\sigma_2, \sigma_3, \sigma_4} - g_{\sigma_1, n\sigma_2, \sigma_3, \sigma_4}|^2 \delta(E_1 + E_2 - E_3 - E_4) \delta(\mathbf{k}_1^{\parallel} + \mathbf{k}_2^{\parallel} - \mathbf{k}_3^{\parallel} - \mathbf{k}_4^{\parallel}), \quad (9)$$

where f and g are direct and exchange scattering amplitudes:

$$f_{\sigma_1, n\sigma_2, \sigma_3, \sigma_4} = \int \psi_3^{\sigma_3*}(\mathbf{x}) \psi_4^{\sigma_4*}(\mathbf{x}') V(\mathbf{x}, \mathbf{x}') \psi_1^{\sigma_1}(\mathbf{x}) \psi_2^{n\sigma_2}(\mathbf{x}') d^3x d^3x'; \quad (10)$$

the expression for g is the same except for \mathbf{x} and \mathbf{x}' interchanged in the first product term. The integrals over \mathbf{x}' and \mathbf{x} extend infinitely in the directions parallel to the surface; lattice periodicity permits, however, for \mathbf{x}' the restriction to the surface unit cell and for \mathbf{x} to the same plus a few neighboring cells (reached by the screened Coulomb interaction). Normal to the surface, both integrals are restricted to a finite number of atomic layers because of screening and the fairly small mean free path of the primary electron.

Since our experiment is performed with fixed solid angles Ω_3 and Ω_4 in the directions of the two outgoing electrons, the observable coincidence event rate (with normalization to the incident current) is obtained from Eq. (9) as

$$I(E_3, E_4, \Omega_3, \Omega_4) = (k_3 k_4 / k_1) W(3, 4), \quad (11)$$

where $k_i = \sqrt{2E_i}$ with $i = 1, 3, 4$.

In view of computing the above expressions, all wave functions are expanded in the form

$$\psi_i^{\sigma_i}(\mathbf{x}) = \sum_{\kappa, \mu, \nu} A_i^{\kappa, \mu, \nu, \sigma_i} \phi_i^{\kappa}(r) \chi_{\kappa\mu}(\theta, \varphi), \quad (12)$$

with $i = 1, \dots, 4$; the $\chi_{\kappa\mu}$ are the usual spin angular functions, the $\phi_i^{\kappa}(r)$ are scalar radial functions, and the coefficients $A_i^{\kappa, \mu, \nu, \sigma_i}$ with atomic layer index ν account for all elastic multiple scattering paths. The screened Coulomb potential [Eq. (8)] is expanded as

$$V(\mathbf{x}, \mathbf{x}') = -\frac{4\pi}{\lambda} \sum_{lm} j_l\left(\frac{ir_<}{\lambda}\right) h_l^{(1)}\left(\frac{ir_>}{\lambda}\right) Y_{lm}^*(\theta, \varphi) Y_{lm}(\theta', \varphi'), \quad (13)$$

where $r_<$ ($r_>$) is the smaller (larger) of $r = |\mathbf{x}|$ and $r' = |\mathbf{x}'|$. Substitution into Eq. (10) yields

$$f_{\sigma_1, n\sigma_2, \sigma_3, \sigma_4} = \frac{-4\pi}{\lambda} \sum_{\substack{\kappa_1, \dots, \kappa_4, \mu_1, \dots, \mu_4 \\ l, m, \nu}} A_3^{\kappa_3, \mu_3, \nu, \sigma_3} A_4^{\kappa_4, \mu_4, \nu, \sigma_4} A_1^{\kappa_1, \mu_1, \nu, \sigma_1} A_2^{\kappa_2, \mu_2, \nu, \sigma_2} R_{34l12} \Omega_{34lm12}, \quad (14)$$

with radial integrals

$$R_{34l12} = \int \phi_{\kappa_3}^*(r) \phi_{\kappa_4}^*(r') j_l\left(\frac{ir_<}{\lambda}\right) h_l\left(\frac{ir_>}{\lambda}\right) \phi_{\kappa_1}(r) \phi_{\kappa_2}(r') dr dr', \quad (15)$$

and Ω denoting angular integrals involving Gaunt coefficients.

In the application of our theory to W(001), the optical potential for the occupied states is a self-consistent LMTO potential cast into the muffin-tin form. For the continuum states it is augmented by an energy-dependent complex inner potential (essentially as in Ref. 18) and a continuous surface potential barrier with image asymptotics. The screening length λ of the Coulomb potential [Eq. (8)] is chosen as 0.7 Å, which corresponds to the Thomas-Fermi screening length for an electron gas with the valence electron density of W. This approximation is acceptable in the present context, since physically reasonable departures of λ from the above value are found to change the calculated coincidence event rate $I(E_3, E_4, \Omega_3, \Omega_4)$ approximately only by a constant factor, i.e., to have, for a given geometry, only little effect on the relative distribution over E_3 and E_4 .

IV. INTERPRETATION OF (SLOW- $e, 2e$) CROSS SECTIONS

Before presenting in some detail experimental and theoretical ($e, 2e$) cross sections from W(001) at low primary energies, we address the question of how information on the electron scattering dynamics and on the electronic structure of the target can be extracted from such ($e, 2e$) data. We recall that at high energies the incident and the ejected electrons are reasonably well described by plane waves, three-dimensional momentum is conserved, and the observed cross section reflects the spectral momentum density of the target electrons. At low primary energies, however, the importance

of multiple elastic scattering both in the primary and in the ejected electron states (LEED and time-reversed LEED states) and the reduction of three-dimensional to only two-dimensional momentum conservation generally preclude such direct information on the electronic structure of the target.

In the following we consider, with the aid of numerical results obtained for W(001), the four relevant one-electron states individually and investigate the role of elastic scattering events of the primary and of the ejected electrons in producing individual features of the fully calculated ($e, 2e$) cross section.

In Fig. 3 we present LEED specular beam spin-averaged intensity versus energy spectra for an unpolarized primary beam incident in the (01) azimuth at polar angles θ in the range from 0° to 88° . The calculated normal incidence spectrum is seen to agree very well with its experimental counterpart.¹⁸ For $15^\circ \leq \theta \leq 45^\circ$, our spectra agree well with experimental data in Ref. 19, and for $45^\circ \leq \theta \leq 70^\circ$ with those presented in Refs. 20 and 21. With θ increasing from 25° upwards, the dominant Bragg maximum at 5 eV is seen to shift towards lower energies. The fine structure on its right-hand side stems from a Rydberg series of surface resonances associated with the emergence threshold of the (01) beam (for details, cf. Refs. 20 and 21). The agreement of the calculated spectra with experimental data suggests that the incident and the two ejected one-electron states are adequately described by our model specifications. In particular, the use of a single one-dimensional surface potential barrier (neglecting corrugation and angular dependence) is acceptable for the present purpose.

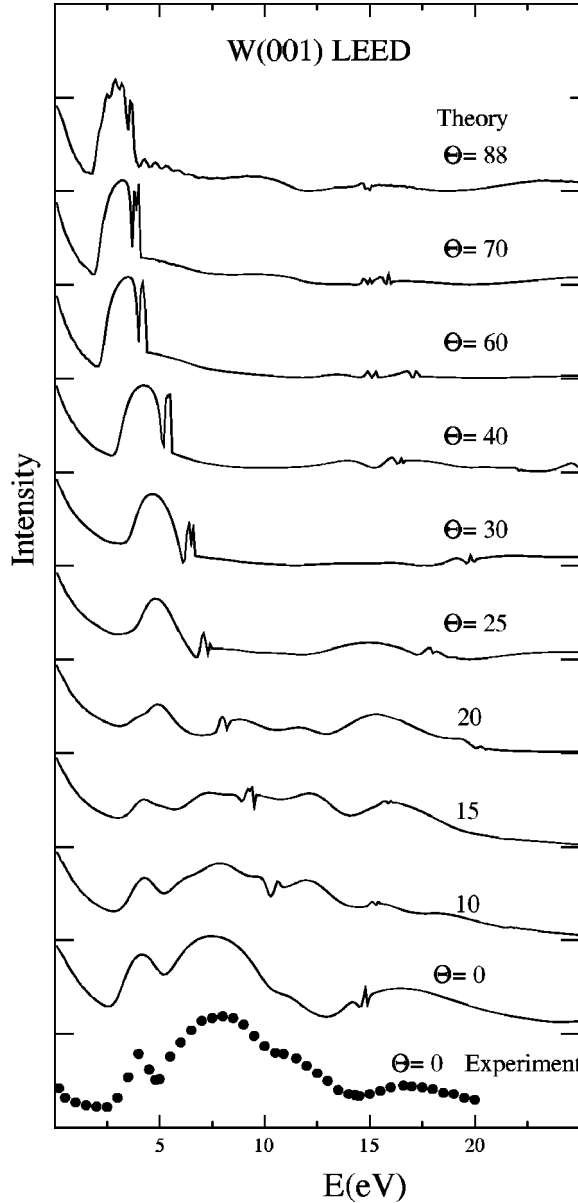


FIG. 3. LEED from W(001): specular beam spin-averaged intensity versus energy curves for an unpolarized beam of unit intensity incident in the (100) azimuth at polar angles as indicated. Solid lines: present theory; dots: experiment (Ref. 18). For each curve, the base line is indicated on the right-hand side and the tick mark on the y axis corresponds to 0.5 (i.e., 50% reflection).

The LEED spectra are of direct relevance for the ($e,2e$) cross section $I(E_3, E_4)$, because a high (low) reflectivity R corresponds to a weak (strong) transmission into the solid. For the primary electron beam at some fixed energy E_1 , $I(E_3, E_4)$ will contain a fixed factor $[1 - R(E_1)]$. Contour plots and energy sharing curves are therefore simply scaled by this factor, which for $E_1 \geq 16$ eV ranges from 0.75 to almost 1 (cf. the normalized specular reflectivities in Fig. 3). In contrast to $R(E_1)$, $R(E_3)$, and $R(E_4)$ influence the shapes of contour plots and of energy sharing curves.

As is well known, the valence electron structure of the semi-infinite crystal can be described by the \mathbf{k}_{\parallel} -resolved density of states $N(E_2, \mathbf{k}_{2\parallel})$, which for short we refer to as “ k -DOS.” The values of E_2 and $\mathbf{k}_{2\parallel}$, which are relevant for

the ($e,2e$) reaction, are determined by conservation of energy and surface-parallel momentum from E_i and $\mathbf{k}_{i\parallel}$ with $i = 1, 3, 4$, which are set by the electron gun and the detectors. Instead of further resolving the k -DOS with respect to atomic layers parallel to the surface, we consider in the following only its most important part, which is the same as the k -DOS of the infinite solid. This bulk k -DOS is closely associated with the usual bulk band structure $E_2(\mathbf{k}_{2\parallel}, k_{2z})$, as we illustrate in Fig. 4. It is important to note that k_{2z} , the momentum component normal to the surface, is not a good quantum number and strictly speaking has no physical relevance for the ($e,2e$) process. It can, however, be of some interest in special cases in which a particular Bloch wave dominates the linear combination, which forms the valence state [2].

In Fig. 4(a) we focus on $\mathbf{k}_{2\parallel} = 0$, which in the coplanar symmetric setup is accessed if $E_3 = E_4$. Our relativistic band structure (for k_{2z} along $\Gamma - H$) agrees with earlier work, where it has been extensively discussed (see, e.g., Refs. 22 and 23). The associated one-dimensional k -DOS is dominated by peaks near E_F , which involve mainly d electrons. If $E_3 \neq E_4$, the relevant bands are along curves in the (k_{2x}, k_{2z}) plane, as is explained in the caption of Fig. 4. Some typical examples of these bands and the associated k -DOS are shown in Fig. 4(b) for our normal incidence geometry. Note that from energy conservation the E_2 values in each of the k -DOS panels of Fig. 4 uniquely correspond to E_4 values. The k -DOS of the relevant occupied states is thus uniquely associated with (E_3, E_4) pairs. A complete k -DOS contour plot in the (E_3, E_4) plane is shown in Fig. 5(a). Along the $E_3 = E_4$ diagonal line, it obviously corresponds to the (smoothed) k -DOS of Fig. 4(a), as it should. As a consequence of the symmetry of the incidence/emission geometry, the k -DOS is mirror symmetric with respect to the $E_3 = E_4$ line. Note that (for fixed E_1) counterdiagonal lines are characterized by fixed values of $E_2 = E_1 - (E_3 + E_4)$. The solid counterdiagonal line indicates the Fermi energy. Figure 5(a) can thus also be viewed as a k -DOS contour plot in the (E_2, k_{2x}) plane with the E_2 and k_{2x} axes along the diagonal and the counterdiagonal, respectively.

The corresponding calculated ($e,2e$) intensity $I(E_3, E_4)$ [cf. Eq. (11), with the solid angle arguments henceforth dropped for brevity, since they are constants for each of our two geometries] is displayed as a contour plot in Fig. 5(b). The mirror symmetry with respect to the $E_3 = E_4$ line is due to the symmetric geometry and to the fact that the primary beam is unpolarized and the emitted electrons are not spin-analyzed. The intensity is seen to be largest for E_2 in the range between E_F and $E_F - 2$ eV, almost zero in the next 2 eV range, and again significant between -4 and -6 eV.

Comparison between the $I(E_3, E_4)$ and the k -DOS contour plots shows that the main ($e,2e$) features occur in regions of high k -DOS, whereas in regions of vanishing k -DOS the ($e,2e$) intensity also vanishes. There is, however, no detailed correspondence. An appreciable k -DOS is therefore a necessary but not sufficient condition. This implies that the incident and ejected electron states play an important role. One may attempt to harness simply the LEED reflectivities of these states. For the ejected electrons, the $\theta = 40^\circ$ spectrum in Fig. 3 has a pronounced peak between 4 and 5 eV. Consequently, the transmission coefficient and, by virtue

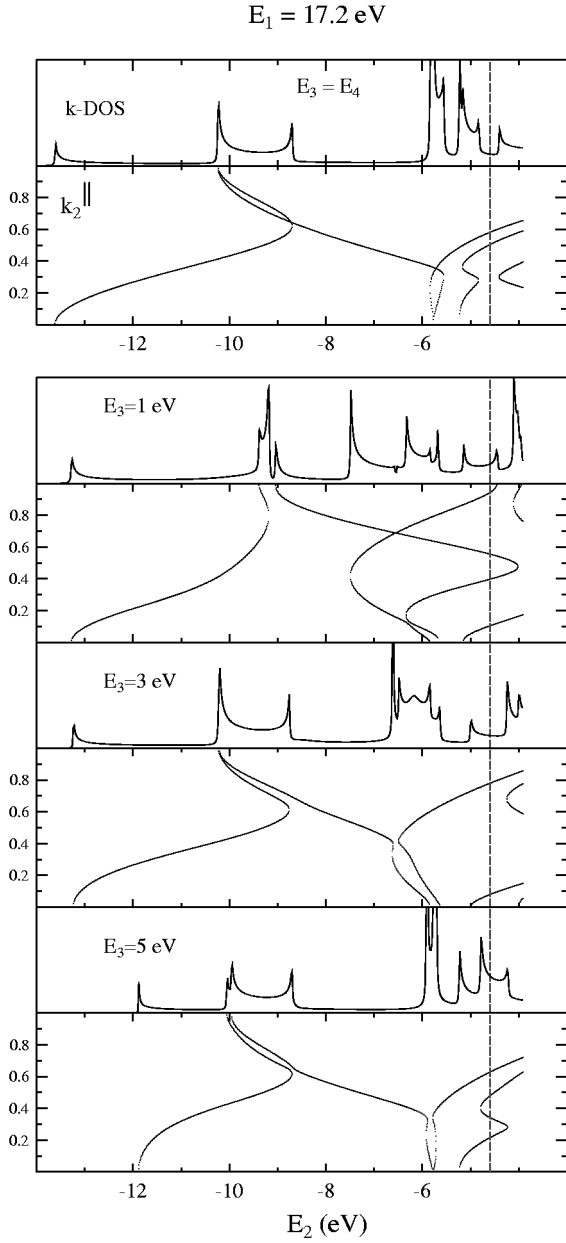


FIG. 4. W bulk band structure along selected relevant \mathbf{k} lines and corresponding density of states “ k -DOS.” The energy E_2 is relative to the vacuum zero, the Fermi energy is marked by the vertical line at -4.6 eV. (a) E_2 versus k_{2z} along ΓH , i.e., for $(k_{2x}, k_{2y}) = (0, 0)$. (b) Projection of $E_2(k_{2x}, k_{2y}, k_{2z})$ onto the (E_2, k_{2z}) plane and k -DOS, with $k_{2y} = 0$ and k_{2x} determined by conservation of energy and surface-parallel momentum — for fixed primary energy $E_1 = 17.2$ eV, $\theta_1 = 0$ (i.e., $\mathbf{k}_{1\parallel} = 0$) and the E_3 values given in the individual panels — as follows: $E_4 = E_1 + E_2 - E_3$ and $k_{2x}(E_2) = k_{3x}(E_3) + k_{4x}(E_4)$, where $k_{3x}(E_3) = (2E_3)^{1/2} \sin \theta_3$ and $k_{4x}(E_4) = -(2E_4)^{1/2} \sin \theta_4$ with detector angles $\theta_3 = \theta_4 = 40^\circ$. Note that we thus have a k -DOS value uniquely associated with each ejected electron pair with energies (E_3, E_4) .

of time reversal, the emission will be reduced if E_3 or E_4 is between 4 and 5 eV. Inspection of Fig. 5(a) shows, however, that intensity values occur at these energies, which in spite of reduction are still substantial.

To get further insight, we found it useful to artificially modify the incident and the ejected electron states, which

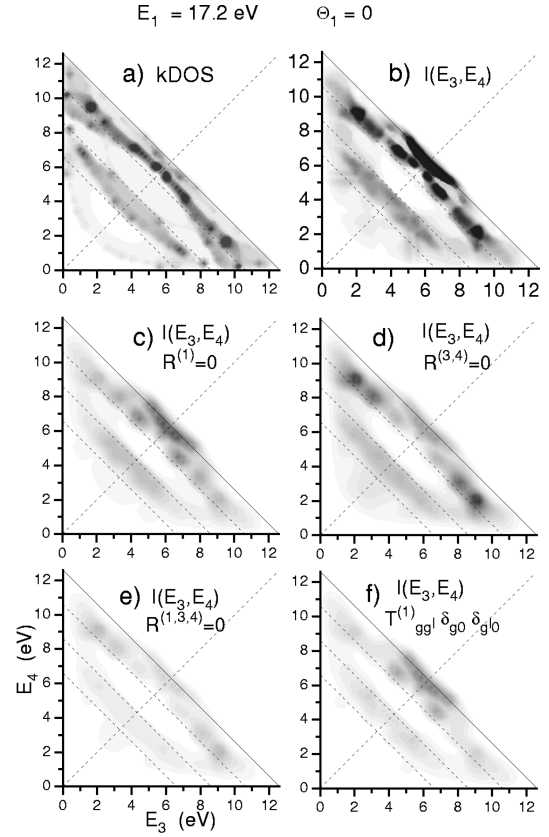


FIG. 5. Contour plots in the (E_3, E_4) plane for $E_1 = 17.2$ eV, $\theta_1 = 0$, and $\theta_3 = \theta_4 = 40^\circ$: (a) k -DOS; the other panels show $I(E_3, E_4)$ calculated (b) with complete elastic multiple scattering, (c) with primary electron back reflection matrix $R^{(1)} = 0$, (d) with $R^{(3,4)} = 0$, (e) with $R^{(1)} = 0$ and $R^{(3,4)} = 0$, (f) neglecting for the primary electron all transmission matrices M_{gg}^{++} except M_{00}^{++} . Along the solid counterdiagonal line $E_2 = E_F$ (Fermi level). The three dashed lines parallel to it correspond to E_2 decreased below E_F in steps of 2 eV.

involve elastic multiple scattering from the ion cores, by selectively switching off elastic scattering amplitudes. To specify these modifications, we briefly recall a key ingredient of layer-KKR theory (for details see, e.g., Chap. 4.3.5 in Ref. 10). Consider a single atomic layer (inside the crystal) with lattice periodicity parallel to the (x, y) plane (the surface plane) and with its internuclear plane at z_a . The wave field incident on this layer is expanded in terms of plane waves $\sum_g \sigma u_g^\sigma e^{i\mathbf{k}_g^\sigma \cdot \mathbf{r}}$, where $\mathbf{k}_g^\sigma = [\mathbf{k}_g^\parallel, \sigma \sqrt{2(E + V_0) - \mathbf{k}_g^\parallel{}^2}]$, the u_g^σ are spinor amplitudes, g enumerates the surface reciprocal-lattice vectors [with $g = 0$ corresponding to $\mathbf{g} = (0, 0)$], and $\sigma = + (-)$ refers to the wave field incident from the left (right) onto the layer (with the z axis being horizontal in the drawing plane). The scattered wave field is analogously expanded with amplitudes v_g^σ , with $\sigma = - (+)$ denoting the field on the left (right) side of the layer. The incoming field is transformed into the outgoing one by the S matrix according to

$$v_g^\sigma = \sum_{\sigma' g'} M_{g g'}^{\sigma \sigma'} u_{g'}^{\sigma'}. \quad (16)$$

We recall that the S -matrix elements $M_{gg'}^{\sigma\sigma'}$ are themselves (2×2) spin matrices. From the above it is clear that $M_{gg'}^{++}$ and $M_{gg'}^{--}$ describe transmission through the layer from left to right and from right to left, respectively, while $M_{gg'}^{+-}$ and $M_{gg'}^{-+}$ account for reflection at the right-hand and at the left-hand side, respectively. For the semi-infinite crystal occupying the half-space $z > 0$, reflection towards the surface can be switched off by setting $M_{gg'}^{-+} = 0$. We apply this to the incoming electron (state 1) and to the ejected electrons (states 3 and 4) separately. For simplicity, we denote in the following the back reflection matrix elements by $R_{gg'}^{(i)}$, with $i = 1, 3, 4$.

The influence on the ($e,2e$) cross section of selectively neglecting back reflection events is illustrated in panels (c)–(e) of Fig. 5. The most notable changes are seen in a counterdiagonal stripe of about 3 eV width just below the Fermi energy. For $R^{(1)} = 0$ [panel (c)], the features far away from the $E_3 = E_4$ diagonal are strongly suppressed, while those nearer the diagonal are essentially preserved although noticeably weakened. For $R^{(3,4)} = 0$ [panel (d)], it is just the opposite. If all three reflection matrices are switched off [panel (e)], only weak traces of all these features are seen to survive. In panel (f), all reflections are taken into account, but for the incoming beam forward transmission events involving nonzero reciprocal-lattice vectors are neglected, i.e., only $M_{00}^{++} \neq 0$. We notice a remarkable similarity with panel (c), where $R^{(1)} = 0$. This implies that the features far from the diagonal in panel (a), which are suppressed in both (c) and (f), require reflection events involving nonzero reciprocal-lattice vectors.

The changes due to neglecting the above elastic scattering events can be displayed more quantitatively by means of energy sharing curves. Because of the symmetry of the present geometry, it suffices to show these only for $E_3 \leq E_4$ (see Fig. 6). Let us focus on the behavior of some typical prominent peaks labeled A–F in Fig. 6(a). Peak A is seen to be still present in panels (b) and (d), but absent in (c). It can thus be interpreted as arising mainly from off-specular (elastic) reflection of the ingoing electron followed by forward inelastic scattering, i.e., a diffraction-loss (DL) feature in traditional EELS terminology. Its absence in panel (f) corroborates this interpretation. In contrast, peak B vanishes in panel (d), but is present in (b), (c), and (f). Forward inelastic scattering followed by reflection (LD) can thus be identified as its main origin. For peaks C and D, off-specular reflection of the ingoing electron is seen to be most important. Their weak presence in panel (e) indicates, however, a significant contribution from direct inelastic scattering (without any reflection events). Peaks E and F involve mainly reflection events of the outgoing electrons 3 and 4, but also off-specular reflection of the primary electron.

In summary, elastic reflection events play a very important role, with some features in the ($e,2e$) energy distribution involving mainly reflections of the ingoing electron, others mainly those of the outgoing electrons. We note that this is in line with what was found in EELS experiments²⁴ and calculations.²⁵ For reflection mode ($e,2e$) at moderate primary energies, elastic reflection events were considered in

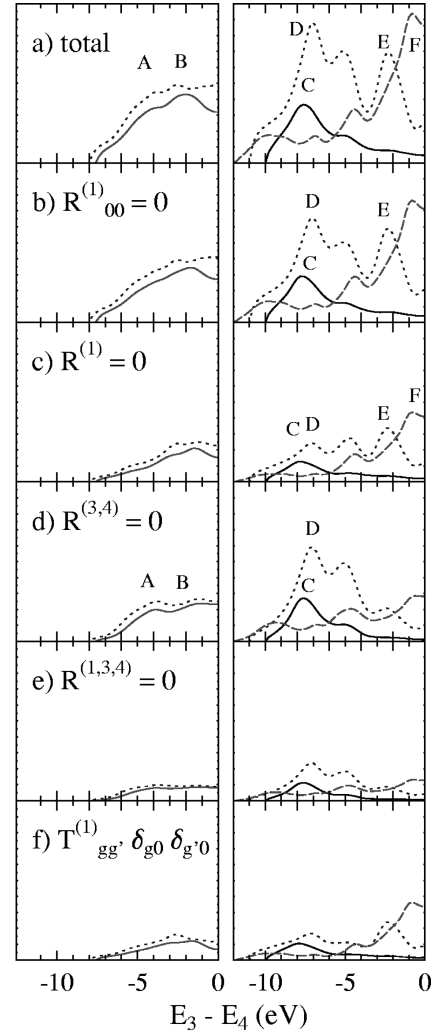


FIG. 6. Energy sharing curves for $E_1 = 17.2$ eV, $\theta_1 = 0$, and $\theta_3 = \theta_4 = 40^\circ$ calculated (a) with complete elastic multiple scattering, (b) with primary electron back reflection matrix element $R_{00}^{(1)} = 0$, (c) with complete matrix $R^{(1)} = 0$, (d) with $R^{(3,4)} = 0$, (e) with $R^{(1)} = 0$ and $R^{(3,4)} = 0$, (f) neglecting for the primary electron all transmission matrices $M_{gg'}^{++}$ except M_{00}^{++} . The selected constant values of $E_3 + E_4$ are as follows: in the right-hand panels, 12 eV (dashed curves), 11 eV (dotted curves), and 10 eV (solid curves); in the left-hand panels, 8 eV (solid curves) and 7.5 eV (dotted curves). Note that the curves are shown only for $E_3 \leq E_4$, since the symmetry of our normal-incidence geometry dictates that for $E_3 \geq E_4$ they are simply mirror symmetric.

detail in Ref. 4. For low-energy ($e,2e$), the importance of elastic reflection of the primary electron was pointed out in Refs. 6 and 26.

The above suggests that one may obtain some more qualitative insight into the collision process, which leads to a particular feature in the ($e,2e$) cross section, by singling out certain specular or nonspecular plane-wave parts from the ingoing and the outgoing one-electron states, and then examining a (hypothetical) collision process involving these plane waves. Since these plane-wave parts are inside the solid, it is essential to take into account the refraction of the primary and the ejected electrons at the surface potential barrier of height V_{0r} , where V_{0r} is the real part of the inner potential.

As is well known, the internal polar angles of incidence (θ'_i) and of exit (θ'_3, θ'_4) are connected with the external ones according to

$$\sin(\theta'_i) = \sqrt{\frac{E}{E + V_{0r}}} \sin(\theta_i) \quad \text{with } i = 1, 3, 4. \quad (17)$$

Refraction is obviously stronger the smaller the energy and the larger the external angles are. With $V_{0r} = 14$ eV, this entails for the presently considered primary energies of around 20 eV that the internal scattering geometry departs significantly from the external one even if one focuses only on specular parts. Moreover, the dependence of θ'_3 and θ'_4 on E_3 and E_4 , respectively, implies that the internal scattering geometry is a different one for each pair (E_3, E_4) . Even for our symmetric normal incidence geometry, in which the primary beam is not refracted, these internal geometries are no longer symmetrical, i.e., $\theta'_3 \neq \theta'_4$, except for the special case $E_3 = E_4$. We note that our results calculated according to Eq. (11) implicitly contain the refraction effects, since our one-electron states are solutions of the Dirac equation in the entire space (i.e., semi-infinite solid and vacuum).

V. EXPERIMENTAL AND THEORETICAL RESULTS

In the following we present and discuss experimental results together with their theoretical counterparts for two coplanar geometries: first, normal incidence and symmetric detector positions; second, grazing incidence and non-symmetric detector positions.

A. Results for normal incidence

In order to make quantitative contact between theory and experiment, the finite energy and angular resolution of the apparatus have to be taken into account. Since their influence is presently quite significant, we illustrate in Fig. 7, for the typical primary energy $E_1 = 17.2$ eV, in some detail the transition from the ideal theoretical contour plot to experimental reality. The effect of an energy-dependent finite lifetime of the bound electron (state 2) is seen by comparing the contour plot in Fig. 7(b) with that in Fig. 7(a). While the cross-section features with E_2 close to the Fermi energy (solid counterdiagonal line) are almost the same, the ones between 4 and 6 eV below E_F in Fig. 7(a) are weakened and broadened due to the comparatively short lifetime in this energy range. Taking into account the experimental energy distribution of the primary electrons [Fig. 7(d)] leads to a smearing out of the features within 2 eV of E_F . Sampling of the ejected electrons over finite emission cones of 22° width around the nominal coplanar directions ($\theta_3 = \theta_4 = 40^\circ$) is seen [in Fig. 7(c)] to produce a broadening of the original features in the counterdiagonal direction. This appears plausible because a given deviation of θ_3 and θ_4 from 40° entails a deviation in $\mathbf{k}_{2\parallel}$, which increases with the difference $E_3 - E_4$. The cone-averaged intensity far away from the diagonal therefore involves bound electrons with more widely distributed values of $\mathbf{k}_{2\parallel}$. The combination of the E_1 and the $\theta_{3,4}$ distributions leads to Fig. 7(e), which agrees quite well with the experimental data in Fig. 7(f). We note that the present geometry (normal incidence and symmetric detec-

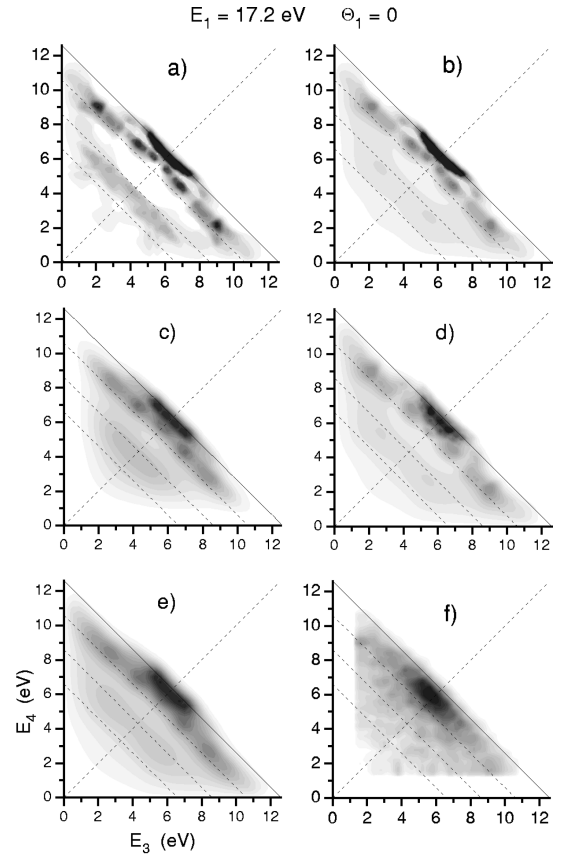


FIG. 7. Contour plots of $I(E_3, E_4)$ for $E_1 = 17.2$ eV, $\theta_1 = 0$: calculations for sharp E_1 and emission angles $\theta_3 = \theta_4 = 40^\circ$ without hole lifetime (a) and with hole lifetime (b); calculations with hole lifetime and for $(\theta_3$ and $\theta_4)$ distributed over a 22° cone (c), for a finite E_1 distribution (d), and for both the (θ_3, θ_4) distribution and the E_1 distribution (e); experiment (f).

tion) dictates mirror symmetry of the contour plots with respect to the $E_3 = E_4$ diagonal line. All the computed plots in fact exhibit this symmetry, while there is a slight asymmetry in the experimental data. As rather obvious reasons for this asymmetry, we identify the counting statistics and some small deviation from the nominal geometry.

In Fig. 8 we show for some further primary energy values experimental contour plots in comparison with calculated ones, which include energy-dependent hole lifetime and averaging over the E_1 distribution and the detection angular cone. For $E_1 = 15.9$ eV, we observe a rather sharp ‘‘central feature’’ stemming from bound electrons close to E_F and $\mathbf{k}_{2\parallel}$ close to zero. For $E_1 = 19.8$ eV, this feature is significantly extended along the counterdiagonal. This trend—into which the results in Figs. 7(e) and 7(f) fit—is seen to continue at $E_1 = 23.7$ eV, but with individual structures along the counterdiagonal emerging.

A more detailed picture of this evolution of features close to E_F is provided by the energy sharing curves in Fig. 9. The agreement between experiment and theory is seen to be rather good except at larger energy differences, where the experimental curves go to zero more rapidly. As one can see directly in the contour plots in Fig. 8, this experimental cut-off occurs if the kinetic energy of one of the ejected electrons reaches 1.8 eV. It is a consequence of our coincidence time

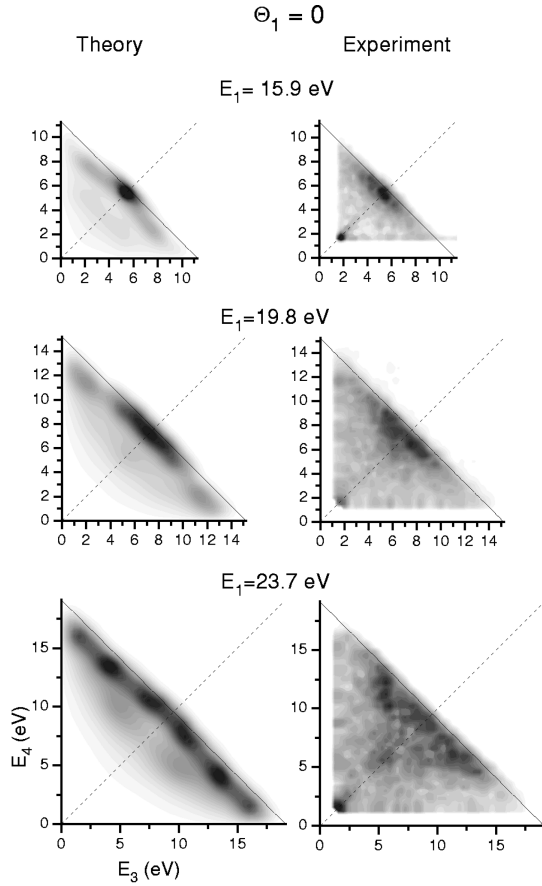


FIG. 8. Contour plots of theoretical and experimental $I(E_3, E_4)$ for $\theta_1 = 0$ (normal incidence) for primary energies E_1 as indicated in the panels.

window of 200 ns. This upper limit for the detectable time-of-flight of an electron implies a lower limit of approximately 1.8 eV for its energy.

It is remarkable that for both E_3 and E_4 very close to 1.8 eV, the experimental data in Fig. 8 exhibit a pronounced cross-section maximum (“dark spot”), which is completely absent in the theoretical results. This feature must therefore be due to a mechanism other than the production of two outgoing electrons by a direct collision of a primary electron with a valence electron. This mechanism should—in addition to the very existence of the dark spot—account for the following two experimentally observed properties: the dark spot increases (relative to the intensities near E_F) (a) with increasing primary energy and (b) (for fixed primary energy) with increasing primary current. We propose the following qualitative explanation. A given primary electron is followed by a second primary electron within a time interval δt , which is small compared to the coincidence time window. Each of these two electrons creates secondary electrons. As is well known (cf., e.g., Ref. 27), the secondary electron emission current is, for a given primary energy, maximal at energies of a few eV, and the size of this maximum increases (for fixed primary current) monotonically with increasing primary energy (up to primary energies of a few hundred eV). The probability for detecting a pair event, which involves one secondary electron generated by the first primary electron and one generated by the second, is therefore largest

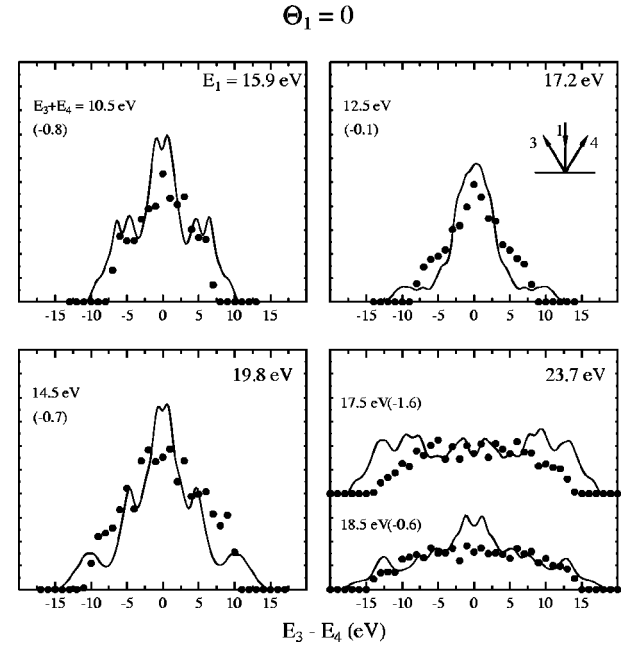


FIG. 9. Energy sharing curves for $\theta_1 = 0^\circ$ and E_1 as indicated in the upper right corner of each panel: calculation (solid lines) and experiment (filled circles) with $I(E_3, E_4)$ averaged over a 1 eV interval centered at the $E_3 + E_4$ values indicated on the left-hand side of each curve. Below each $E_3 + E_4$ value, the corresponding value of E_2 relative to the Fermi level, which is simply obtained from energy conservation as $E_1 - 4.6 - (E_3 + E_4)$, is given in brackets. Both the theoretical and experimental cross sections are in arbitrary units.

for E_3 and E_4 close to the experimental cutoff energy of 1.8 eV. Furthermore, the probability of this “accidental event” increases monotonically with the primary energy. Since the probability for the true event does not grow in such a monotonic way, the accidental-event probability increases relative to the true-event probability. This is in accordance with the observed behavior (a) of the dark spot. If at fixed primary energy the primary current is increased, the true-event intensity grows linearly, whereas the accidental-event intensity increases quadratically. Consequently, the latter grows relative to the former, and the dark spot should become more prominent. The mechanism, which involves two secondary electrons generated by two different primary electrons, thus also explains the behavior (b) of the dark spot.

Another feature, which is absent in the calculated results, is the maximum near $E_3 = E_4 = 6$ eV in the experimental data for $E_1 = 23.7$ eV and, somewhat less pronounced, for $E_1 = 19.8$ eV. As a possible mechanism we suggest energy loss of the primary electron from E_1 to an energy E'_1 , which does not depend on the value of E_1 , and subsequent collision with a valence electron and pair ejection. From the sequence of experimental contour plots shown, the cross-section peak near $E_3 = E_4 = 6$ eV would then consistently correspond to an energy E'_1 of about 16 eV. A clue to the nature of this mechanism is provided by the LEED spectrum (Fig. 3) for $\theta = 40^\circ$, which exhibits a series of surface resonances just around 16 eV. We thus obtain the following picture: the primary electron gets inelastically scattered into a surface resonance, which in turn decays by scattering with a valence electron (from the vicinity of the Fermi energy), thus produc-

ing the observed correlated electron pair with $E_3 = E_4 = 6$ eV. This interpretation is experimentally corroborated by the finding that the above cross-section peak is suppressed by oxygen adsorption.

Since our theoretical method contains the screening length λ of the Coulomb interaction as a parameter (with the value 0.7 \AA underlying all results shown in this work), we explored the influence of physically reasonable variations of λ by performing some additional calculations using the values 0.35 and 1.4 . We found that the absolute values of $I(E_3, E_4)$ increase with increasing screening length, i.e., longer range of the interaction, with maximal-intensity ratios $9:3:0.6$ for the λ values 1.4 , 0.7 , and 0.35 \AA . The relative intensities of the features are, however, almost the same, i.e., the normalized contour plots look almost identical.

B. Results for grazing incidence

For the geometry, we refer to Fig. 1(b) and the inset in the top right-hand panel of Fig. 12. The primary electrons impinge on the surface at a polar angle $\theta_1 = 88^\circ$ (with respect to the surface normal) and the ejected electrons are detected coplanar at polar angles $\theta_3 = 47^\circ$ and $\theta_4 = 33^\circ$ with azimuths such that 4 is in the same quadrant as 1, and 3 in the other. The scattering angles relative to the direction of the incident beam are thus $\Theta_3 = 45^\circ$ and $\Theta_4 = 125^\circ$, i.e., one electron of the pair is forward-scattered, the other backward. (In the normal incidence case dealt with above, $\Theta_3 = \Theta_4 = 140^\circ$, i.e., both electrons are backward-scattered.) With regard to the internal scattering geometries discussed towards the end of Sec. IV, we note that for energies E_1 around 20 eV , refraction at the surface [cf. Eq. (17)] changes the external angle $\theta_1 = 88^\circ$ into an internal θ'_1 around 50° . The internal incidence on the planes of ion cores is therefore far from grazing.

In Fig. 10 we show, for $E_1 = 17.2 \text{ eV}$, the k -DOS of the bound electrons (state 2) and the $(e, 2e)$ distribution $I(E_3, E_4)$ as it goes from ideal theory to experiment. Comparison between panels *a* and *b* essentially confirms what we found for normal incidence (cf. Fig. 5): a finite k -DOS is necessary, but the Coulomb matrix elements involving also the other three states can have substantial influence. Most notably, the strong k -DOS features around $E_3, E_4 = (2, 9.5)$ and $(9, 1)$ do not show up at all in the cross section. Finite hole lifetime [Fig. 10(c)] again weakens features further away from E_F and the sampling over the emission cones [Fig. 10(e)] produces a concentration towards $E_3 = E_4$. Comparison with experiment [Fig. 10(f)] shows very good agreement with regard to the dominant feature around $(E_3, E_4) = (5, 6)$. The experimental peak around $(4.5, 7)$ is reproduced by the calculations in panels (c) and (d), but has been smeared out by the angular averaging in panel (f). As observed and discussed above for normal incidence, the experimental data in addition exhibit a “background spot” near $(E_3, E_4) = (2, 2)$, and a cutoff for E_3 or E_4 below about 2 eV , which is due to the 200 ns time window used for the coincidence condition.

In Fig. 11 we show for some further primary energy values experimental contour plots in comparison with calculated ones, which include energy-dependent hole lifetime and averaging over the E_1 distribution and the detection angular

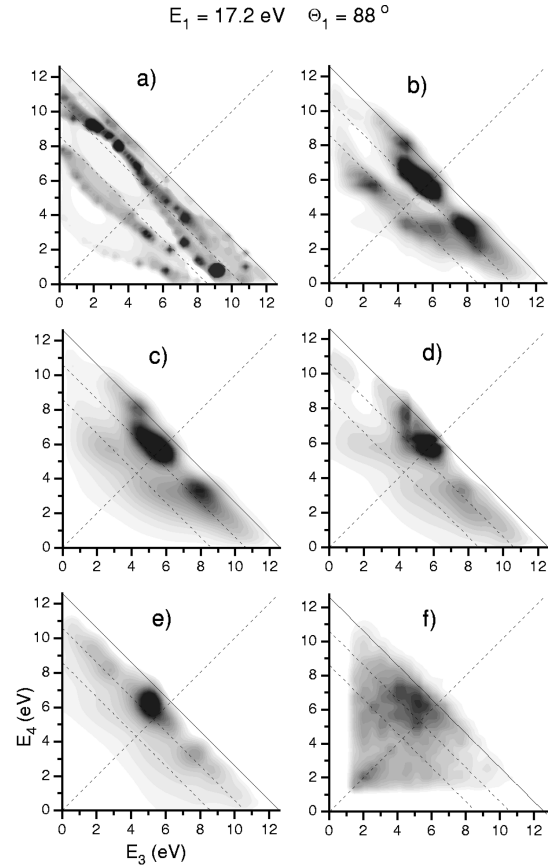


FIG. 10. Contour plots in the (E_3, E_4) plane for $E_1 = 17.2 \text{ eV}$ and the grazing incidence ($\theta_1 = 88^\circ$) geometry sketched in Fig. 1(b): (a) k -DOS; panels (b)–(e) show $I(E_3, E_4)$ calculated without hole lifetime (b), with hole lifetime (c), with hole lifetime for a finite E_1 distribution (d) and for $(\theta_3$ and $\theta_4)$ distributed over a 22° cone (e); the experimental data are shown in panel (f).

cones. For $E_1 = 16.1 \text{ eV}$, theoretical and experimental results agree rather well, both being dominated by a peak centered around $(E_3, E_4) = (5, 6)$. For $E_1 = 19.8 \text{ eV}$, however, the calculated distribution looks rather different from the experimental one, with strong features of the latter absent in the former. One of these, close to E_F near $(E_3, E_4) = (8, 7)$, can be attributed to a surface state and will be discussed in detail below. Another one is a broad peak around $(5, 6.5)$ superimposed on the $(5, 6)$ feature also present in the calculated plot. A broad peak around the same energies $(5, 6.5)$ is seen for $E_1 = 23.8 \text{ eV}$ to dominate the measured distribution and to be absent in the calculated one. We interpret this broad peak in the same way as the $(6, 6)$ feature observed for normal incidence (see Fig. 6 and the above discussion): energy loss of the primary electron from E_1 to an energy E'_1 , which does not depend on the value of E_1 , and subsequent collision with a valence electron and pair ejection.

Due to the increase of multiple energy losses and background with increasing primary energy, comparing theory (which contains only single collision events) and experiment by means of gray-scale contour plots becomes less adequate. Instead, one should rather employ energy sharing curves. Such are shown in Fig. 12 for a sequence of primary energies. We recall that each point in these curves is obtained by

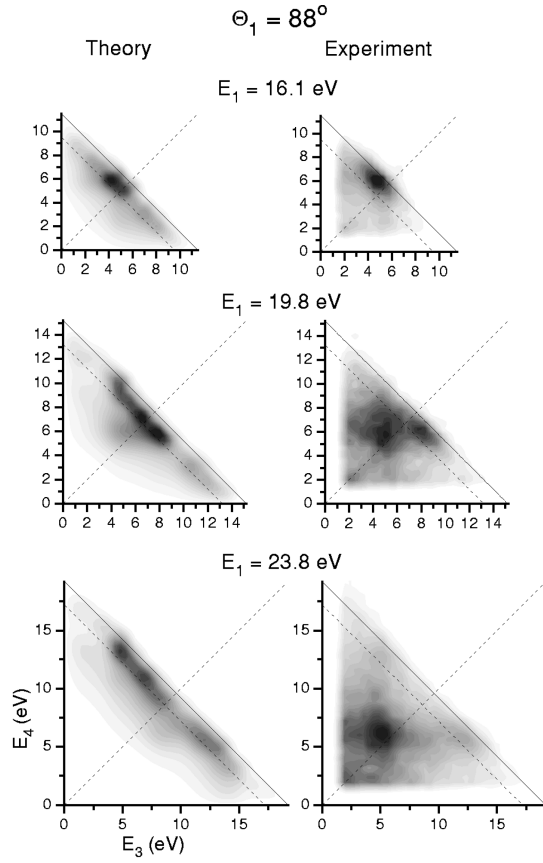


FIG. 11. Contour plots of theoretical and experimental $I(E_3, E_4)$ for $\theta_1 = 88^\circ$ (grazing incidence) for primary energies E_1 as indicated in the panels.

summing $I(E_3, E_4)$ over an $E_3 + E_4$ interval of 1 eV centered at the nominal value of $E_3 + E_4$. All the curves are quite asymmetric with respect to $E_3 - E_4 = 0$, which is to be expected from the absence of symmetry in the scattering geometry.

For $E_1 = 16.1$ eV, experiment and theory exhibit a dominant peak at $E_3 - E_4 = -2.5$ eV. To understand its origin, we performed additional calculations with elastic reflection matrix elements selectively switched off. While specular and nonspecular reflection of the primary electron and specular reflection of the ejected electrons turned out to be unimportant, nonspecular reflections of the ejected electrons play a crucial role. One can therefore visualize the underlying mechanism as a forward collision event between the primary and valence electron followed by nonspecular reflection events, i.e., a loss-diffraction (LD)-type process in traditional terminology. Furthermore, direct transmission of the primary electron through the atomic layers by far dominates transmission with deflections involving surface reciprocal-lattice vectors. The key to understanding these findings lies in the fact that the direct collision cross section is large for small momentum transfer, i.e., if both of the scattered electrons move in the forward direction, and is small if one of them goes backward. Since in the present geometry (cf. the inset in the top right-hand panel of Fig. 12) one ejected electron is backward-scattered, direct collision without any reflection has a low probability. For collisions with specularly reflected primary electrons, 4 is still backwards and hence

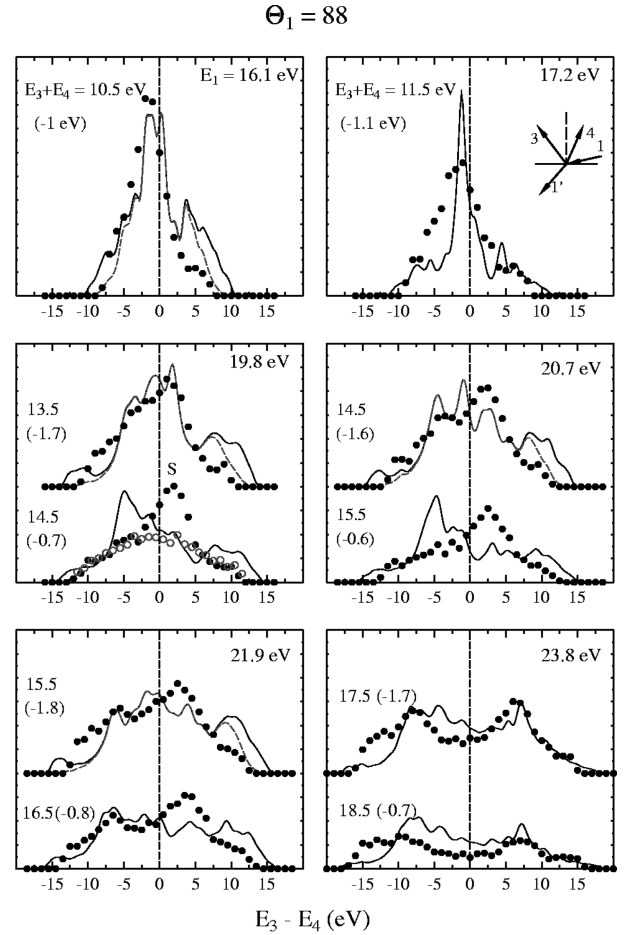


FIG. 12. Energy sharing curves for $\theta_1 = 88^\circ$ and E_1 as indicated in the upper right corner of each panel. The presentation is analogous to the one in Fig. 9. In the panel for $E_1 = 19.8$ eV, the additional empty circles represent data obtained after adsorption of oxygen on W(001). The dashed lines in regions of large energy differences represent an *ad hoc* smooth truncation of the calculated curves.

the cross section is small. Collision of the directly transmitted beam with valence electrons produces mainly two electrons going forward, i.e., into the crystal, and their subsequent reflection, with one of them nonspecular, channels them right into the detectors. This sequence has therefore a high probability.

Analysis of prominent peaks in the other calculated energy sharing curves revealed the same underlying physical mechanism. In particular, this also holds for the strong peak towards the “far right” of most of the calculated energy sharing curves, which falls into the experimental cutoff region. For all the peaks investigated, direct transmission of the primary electron is vital, whereas deflection by a reciprocal-lattice vector plays a very minor role. Finally, we would like to point out that switching off certain reflection or transmission matrices does not necessarily reduce $I(E_3, E_4)$ or leave it unchanged, but it can also enhance it. The latter is, however, not surprising, since the elastic multiple scattering is coherent, and omission of an amplitude, which destructively interferes with some other, leads to an enhancement of I .

Within the cutoff limits, good overall agreement between experiment and theory is seen for most of the curves, but there are some discrepancies. A substantial one occurs for primary energy $E_1 = 19.8$ eV and $E_2 = -0.7$ eV around $E_3 - E_4 = 2$ eV: a strong experimental peak (labeled by S) contrasts with a small calculated shoulder. The disappearance of this peak in experiment upon oxygen adsorption suggests that it might originate from a surface state or resonance. In fact, photoemission experiments on W(001) (Ref. 28) revealed three surface resonances with energies fairly slightly dispersing with \mathbf{k}_{\parallel} , but intensities varying quite strongly (cf. Fig. 6 of Ref. 28). To make closer contact with these data, we therefore need to know $\mathbf{k}_{2\parallel}$ of the valence electron associated with our peak S . From energy and parallel-momentum conservation one easily obtains $\mathbf{k}_{2\parallel} = (k_{2x}, 0) = (-0.95g, 0)$, where g is the surface reciprocal-lattice constant. In the first Brillouin zone, we thus find $k_{2x} + g = 0.05g$, which is about 0.1 \AA^{-1} . At this value, the photoemission data of Ref. 28 exhibit a strong surface resonance at energy -0.4 eV relative to E_F , and a weaker one at -0.8 eV. Our peak S is thus clearly associated with the -0.8 eV resonance. Due to our data collection over a 1 eV interval of $E_3 + E_4$ and consequently of E_2 between -1.2 and -0.2 eV, S also contains contributions from scattering with the -0.4 eV resonance.

The absence of S in the calculated curves is due to the Bloch wave matching method employed for the valence state. Since this method requires using a real crystal potential—with the imaginary inner potential part V_{0i} taken into account by a subsequent convolution with a Lorentzian—surface states have very sharp energies. Consequently they are most likely not to be found in the presently used computationally viable energy grid. To explore S further, we employed a Green-function method,¹⁶ which *a priori* incorporates lifetime broadening, to calculate the layer- and \mathbf{k}_{\parallel} -resolved density of states of the valence electrons. For \mathbf{k}_{\parallel} around 0.1 \AA^{-1} , we thereby found two surface features at the above energies. With increasing E_1 , the measured surface state peak in Fig. 12 is seen to move from 2 eV to 4.5 eV (at $E_1 = 21.9$ eV) and becomes less prominent.

The influence of physically reasonable variations of the screening length λ of the Coulomb interaction on the calculated $I(E_3, E_4)$ was found to be similar at grazing incidence as above at normal incidence. While the absolute values of $I(E_3, E_4)$ increase with increasing screening length, the relative intensities and hence the contour plots are almost the same.

VI. CONCLUSION

We have measured and calculated cross sections of $(e, 2e)$ in the reflection mode from the W(001) surface for primary electrons with energies below 25 eV at normal and at grazing incidence. Our theory describes, in the spirit of a distorted-wave Born approximation with exchange, a single collision event between the primary electron and a valence electron resulting in two electrons leaving the crystal. For each of the four-ingredient one-electron states, elastic multiple scattering by the ion cores is fully taken into account.

For valence electron energies within a few eV of the Fermi energy, we have found good overall agreement between experiment and theory. Since the latter involves only a single direct collision between the projectile and a target electron, this agreement implies that such direct collisions are the dominant origin of the two electrons observed experimentally.

Additional calculations, in which selected elastic scattering matrix parts for either the primary or the detected electrons, or for both, are deliberately discarded, yielded more insight into the mechanisms underlying particular cross-section features. Generally, elastic reflection was found to be very important. More specifically, certain features mainly require elastic reflections in the primary electron state, while for others reflection in one of the ejected electron states is indispensable.

Our experimental data reveal occupied surface states within 1 eV of the Fermi level, in accordance with our density of states calculation and with earlier photoemission data. To obtain the corresponding $(e, 2e)$ features theoretically, the Bloch wave matching treatment of the valence electrons in our present formalism has to be replaced by a Green-function method, which incorporates lifetime broadening from the start rather than taking it into account by a Lorentzian convolution.

In conclusion, our results ensure a bright future for very low-energy $(e, 2e)$ spectroscopy in the reflection mode from solid surfaces. Although it is theoretically far more complicated than high-energy $(e, 2e)$ spectroscopy, experimental data can be quantitatively reproduced by numerical calculations and interpreted in terms of underlying physical mechanisms. The surface sensitivity, which we found, suggests usefulness for studying ultrathin film and multilayers.

ACKNOWLEDGMENT

It is our pleasure to thank Udo Rucker for his valuable assistance in the graphical presentation of the calculated results.

¹S.A. Canney, M. Vos, A.S. Kheifets, N. Clisby, I.E. McCarthy, and E. Weigold, *J. Phys.: Condens. Matter* **9**, 1931 (1997).

²M. Vos, Z. Fang, S.A. Canney, A.S. Kheifets, I.E. McCarthy, and E. Weigold, *Phys. Rev. B* **56**, 963 (1997).

³H. Gollisch, D. Meinert, Xiao Yi, and R. Feder, *Solid State Commun.* **102**, 317 (1997).

⁴J. Berakdar and M. P. Das, *Phys. Rev. A* **56**, 1403 (1997).

⁵A.S. Kheifets, S. Iacobucci, A. Ruocco, R. Camilloni, and G. Stefani, *Phys. Rev. B* **57**, 7360 (1998).

⁶O.M. Artamonov, S.N. Samarin, and J. Kirschner, *Phys. Rev. B* **51**, 2491 (1995).

⁷J. Kirschner, O.M. Artamonov, and S.N. Samarin, *Phys. Rev. Lett.* **75**, 2424 (1995).

⁸S. Iacobucci, L. Marassi, R. Camilloni, S. Nannarone, and G. Stefani, *Phys. Rev. B* **51**, 10 252 (1995).

⁹G. Stefani, *Can. J. Phys.* **74**, 10 525 (1995).

¹⁰*Polarized Electrons in Surface Physics*, edited by R. Feder (World Scientific, Singapore, 1985).

- ¹¹R. Feder and J. Henk, in *Spin-Orbit Influenced Spectroscopies of Magnetic Solids*, Lecture Notes in Physics Vol. 466, edited by H. Ebert and G. Schütz (Springer, Berlin, 1996), p. 85.
- ¹²B. Ackermann and R. Feder, *Solid State Commun.* **54**, 1077 (1985).
- ¹³E. Tamura, W. Piepke, and R. Feder, *Phys. Rev. Lett.* **59**, 934 (1987).
- ¹⁴E. Tamura, R. Feder, B. Vogt, B. Schmiedeskamp, and U. Heinzmann, *Z. Phys. B* **77**, 129 (1989).
- ¹⁵E. Tamura and R. Feder (unpublished).
- ¹⁶S.V. Halilov, E. Tamura, H. Gollisch, D. Meinert, and R. Feder, *J. Phys.: Condens. Matter* **5**, 3859 (1993).
- ¹⁷G.D. Carse and D.W. Walker, *J. Phys. B* **6**, 2529 (1973).
- ¹⁸H.J. Herlt, R. Feder, G. Meister, and E. Bauer, *Solid State Commun.* **38**, 973 (1981).
- ¹⁹E.G. McRae, D.T. Pierce, G.C. Wang, and R.J. Celotta, *Phys. Rev. B* **24**, 4230 (1981).
- ²⁰J.M. Baribeau, J. Lopez, and J.C. Le Bosse, *J. Phys. C* **18**, 3083 (1985).
- ²¹J.M. Baribeau, J.D. Carette, P.J. Jennings, and R.O. Jones, *Phys. Rev. B* **32**, 6131 (1985).
- ²²N.E. Christensen and B. Feuerbacher, *Phys. Rev. B* **10**, 2349 (1974).
- ²³R. Feder and K. Sturm, *Phys. Rev. B* **12**, 537 (1975).
- ²⁴D. Rebenstorff, H. Ibach, and J. Kirschner, *Solid State Commun.* **56**, 885 (1985).
- ²⁵Xiao Yi, Niu Jier, Herbert Gollisch, and Roland Feder, *Solid State Commun.* **99**, 283 (1996).
- ²⁶O.M. Artamonov, S.N. Samarin, and J. Kirschner, *Appl. Phys. A: Mater. Sci. Process.* **65**, 535 (1997).
- ²⁷O. Hachenberg and W. Brauer, *Adv. Electron. Electron Phys.* **11**, 413 (1959).
- ²⁸S. Weng, E.W. Plummer, and T. Gustafsson, *Phys. Rev. B* **18**, 1718 (1978).